DIRECT NUMERICAL SIMULATION OF A THREE-DIMENSIONAL NATURAL-CONVECTION FLOW IN A DIFFERENTIALLY HEATED CAVITY OF ASPECT RATIO 4

M. Soria , F. X. Trias , C. D. Pérez-Segarra & A. Oliva

Published online: 17 Aug 2010.

Submit your article to this journal ↗

Article views: 165

View related articles ↗

Citing articles: 23 View citing articles ↗

Taylor & Francis
Taylor & Francis Group

DIRECT NUMERICAL SIMULATION OF A THREE-DIMENSIONAL NATURAL-CONVECTION FLOW IN A DIFFERENTIALLY HEATED CAVITY OF ASPECT RATIO 4

M. Soria, F. X. Trias, C. D. Pérez-Segarra, and A. Oliva

Centre Tecnològic de Transferència de Calor, Universitat Politècnica de Catalunya, Terrassa, Barcelona, Spain

The majority of the direct numerical simulations of turbulent and transition natural-convection flows in cavities assume two-dimensional behavior. To investigate the effect of the three-dimensional fluctuations, a complete direct numerical simulation has been carried out, in a cavity with aspect ratio 4, $Ra_z = 6.4 \times 10^8$, and $Pr = 0.71$, using a low-cost PC cluster. A description of the parallel algorithm and the methodology used to verify the code and the accuracy of the statistics obtained is presented. The main features of the two- and three-dimensional flows are described and compared. Several first- and second-order statistic distributions have been evaluated, including the Reynolds stress tensor. Significant differences are observed between the second-order statistics of the two- and three-dimensional simulations.

1. INTRODUCTION

Natural convection in two-dimensional (2-D) and three-dimensional (3-D) parallelepipedic enclosures has been the subject of numerous studies. The majority of them can be classified into three groups: (1) cavities in which the flow is due to internal heat generation, (2) cavities heated from below (Rayleigh-Benard configuration), and (3) differentially heated cavities (DHC), the situation that here is under consideration.

A schema of a general DHC problem is presented in Figure 1. Two opposite vertical walls of the cavity, $y = 0$ and $y = L_y$, are kept isothermal at temperatures T_c and $T_h > T_c$. The horizontal walls $z = 0$ and $z = L_z$ can be either adiabatic ($\partial T / \partial z = 0$) or perfectly conducting (i.e., with a linear temperature profile between the hot and the cold temperatures). Here, these variants will be respectively denominated AHW and PCHW. If the Boussinesq approximation is used, the DHC

NOMENCLATURE

A_x, A_z	height and depth aspect ratios	Ra_z	Rayleigh number based on cavity
e	local kinetic energy		height
E	volume integrated kinetic energy	t	time
$\overline{E}_g$	averaged kinetic energy generation	t_o	beginning of integration period
	rate	T	temperature
$\overline{E}_d$	averaged kinetic energy dissipation	T_c	cold wall temperature
	rate	T_h	hot wall temperature
$\mathbf{f}$	body force	V	volume
L	length	x, y, z	coordinates
N	number of nodes	α	thermal diffusivity
Nu	Nusselt number	β	thermal expansion coefficient
p	dynamic pressure	γ	grid concentration parameter
ph, pl	spatial and temporal order of	Δt	time step
	accuracy	Δt_a	time-averaging integration period
P_r	Prandtl number	$\Delta T =$	$T_h - T_c$
g	gravitational acceleration	$\Delta x, \Delta y, \Delta z$	mesh size
$\mathbf{u}$	velocity	ν	kinematic viscosity
Ra_y	Rayleigh number based on cavity	χ	generic unknown
	width	$\phi(\mathbf{u}) =$	$(\nabla \mathbf{u} + \nabla \mathbf{u}^t) : \nabla \mathbf{u}$

problem is governed by $\mathrm{Ra}_z = \beta \Delta T L_z^3 g / \alpha \nu$ and $\mathrm{Pr} = \nu / \alpha$ numbers and the geometric aspect ratios $A_z = L_z / L_y$ (height aspect ratio) and $A_x = L_x / L_y$ (depth aspect ratio).

In the case of 3-D cavities, the vertical planes that close the cavity in the depth direction, orthogonal to the main flow ($x = 0$ and $x = L_x$), can be considered adiabatic solid walls ($\mathbf{u} = 0$, $\partial T / \partial x = 0$), or a periodic behavior can be assumed, $\chi(x, y, z, t) = \chi(x + L_x, y, z, t)$. Here, these variants will be respectively denominated solid vertical walls (SVW) and periodic vertical boundary conditions (PVBC). The SVW variant forces the flow to be 3-D, independent of the Ra number. Nonslip boundary condition ($\mathbf{u} = 0$) is always used for the other four planes.

A summary of previous numerical studies of DHC flows of air ($\mathrm{Pr} = 0.71$) that are relevant in our context is presented in the next paragraphs. All of them solve directly the incompressible Navier-Stokes equations (without turbulence models), using air as working fluid and, except where mentioned, the Boussinesq approximation.

Steady-State Flows

The square cavity with AHW is a very well known configuration often used to test Computational Fluid Dynamics (CFD) codes. The original benchmark formulation [1] was for $10^3 \leq \mathrm{Ra}_z \leq 10^6$. A multigrid method was used in [2] to solve the problem with meshes up to 640×640. Latter, solutions for the full range of steady-state solutions ($\mathrm{Ra}_z \leq 10^8$) were obtained using various methods [3–5]. The 3-D cubic cavity ($A_x = A_z = 1$) with AHW and SVW is also a well-known configuration, but has received comparatively less attention [6, 7]. For cavities with large height aspect ratios, in a certain range of Ra numbers [8–10], a steady-state multicellular flow is obtained.
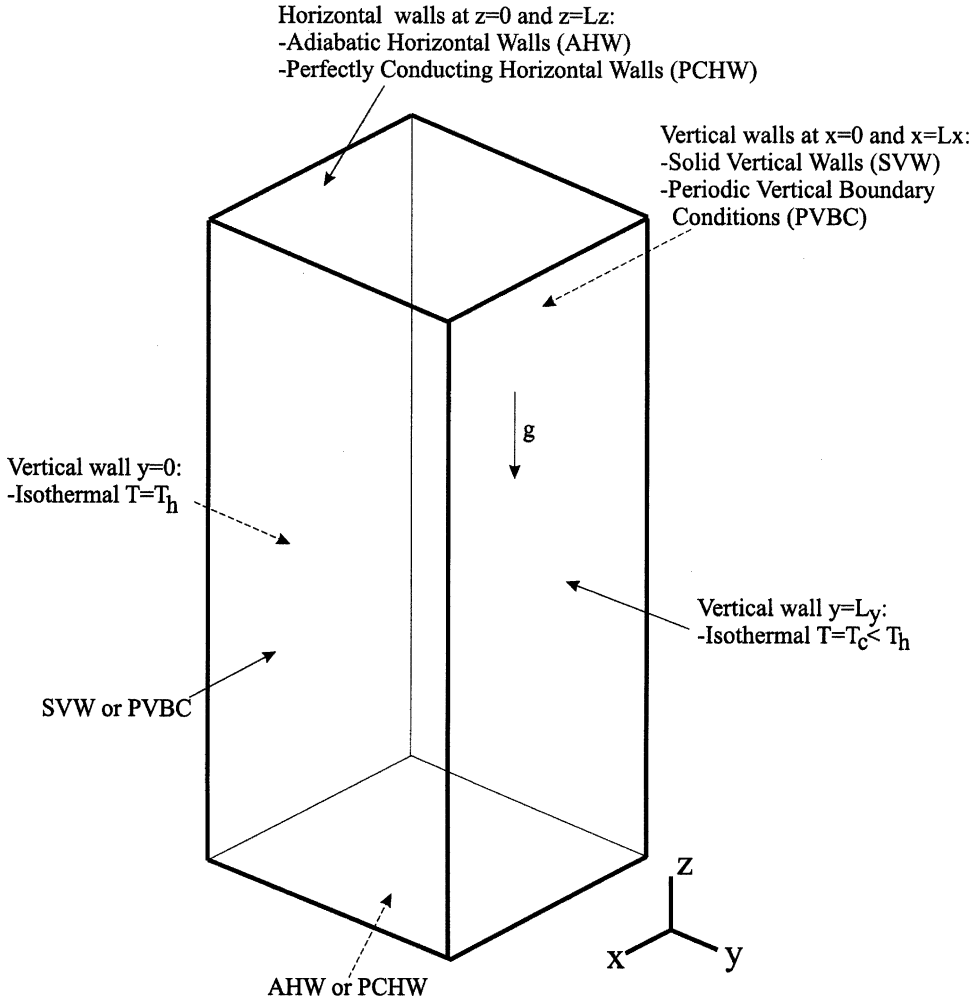
Horizontal walls at z=0 and z=Lz:
-Adiabatic Horizontal Walls (AHW)
-Perfectly Conducting Horizontal Walls (PCHW)

Vertical walls at x=0 and x=Lx:
-Solid Vertical Walls (SVW)
-Periodic Vertical Boundary
 Conditions (PVBC)

g

Vertical wall y=0:
-Isothermal T=T_h

Vertical wall y=L_y:
-Isothermal T=T_c< T_h

SVW or PVBC

z

x   y

AHW or PCHW

Figure 1. General DHC problem.

Time-Dependent Two-Dimensional Flows

Beyond a critical Rayleigh number, the DHC flows become time-dependent (periodic, chaotic, and eventually fully turbulent), even with steady boundary conditions. The PCHW configuration is more unstable than the AHW, due to the presence of high-temperature areas at the bottom of the cavity. Its transition to nonsteadiness was studied in [11], obtaining a critical number of $Ra_z = 2.109 \times 10^6$, later confirmed by Henkes [12]. For the square AHW cavity, Le Quéré et al. [13] evaluated the critical number as $Ra = 1.82 \pm 0.01 \times 10^8$ and studied the time-dependent chaotic flows up to $Ra = 10^{10}$. For the case of cavities with AHW and $A_z = 4$ [14], there is a Hopf bifurcation at $Ra_z = 1.03 \times 10^8$, and chaotic behavior is first observed at $Ra_z = 2.3 \times 10^8$. Two-dimensional "turbulent" flows have been studied by Farhangnia et al. [15], who carried out a direct simulation for

$Ra_z = 6.4 \times 10^{10}$, and by Xin and Le Quéré [14], who studied the situations with $Ra_z = 6.4 \times 10^8$, 2×10^9, and 10^{10}, recording statistics of the flow for $Ra_z = 2 \times 10^9$ and 10^{10}. Recently, the AHW cavity with $A_z = 8$, with $Ra_y = 3.4 \times 10^5$ (unsteady), has been chosen as a test problem [16]. For this configuration, the critical Ra_y number for the transition to unsteadiness is $Ra_y = 3.0619 \times 10^5$. Time-dependent 2-D flows have also been studied without using the Boussinesq approximation [17,18], for Rayleigh numbers up to 10^{10} and various aspect ratios.

Time-Dependent Three-Dimensional Flows

The transition from 3-D steady to 3-D time-dependent flows was considered, for the case of a PCHW cubic cavity with SVW in [19], assuming symmetry. The critical Ra number was estimated to be between 2.25×10^6 and 2.35×10^6, larger than the equivalent critical number of a 2-D cavity. An oscillatory flow was studied [20] in the same conditions, without assuming symmetry, for $Ra = 8.5 \times 10^6$. For the case of the AHW cubic cavity ($A_z = A_x = 1$, AHW, SVW), the transition to unsteadiness was studied in [21], assuming symmetry too. The critical Ra number obtained was between 2.5×10^8 and 3×10^8. However, the same configuration was later studied without assuming symmetry [22], obtaining a nonsymmetric transition for $Ra = 3.19 \times 10^7$, significantly lower than in the equivalent 2-D case. The direct simulation of a turbulent flow with $Ra = 10^{10}$ was carried out in [23], using a $62 \times 122 \times 62$ mesh.

Transition from Two-Dimensional to Three-Dimensional Flows

In a general DHC problem with PVBC, where the boundary conditions do not force the flow to be 3-D, there are three possible flow configurations: 2-D steady, 2-D unsteady, and 3-D unsteady. A question relevant in our context is whether there is a range of Rayleigh numbers in which the flow is 2-D but unsteady, that is, if the transitions to unsteadiness and three-dimensionality are simultaneous.

This was considered in detail in [24], for square cavities ($A_z = 1$) with AHW and PCHW, using PVBC boundary conditions. In both cases, it was found that 3-D perturbations are less stable than 2-D perturbations, concluding that the assumption of two-dimensionality is not correct (in time-dependent square DHC). A 3-D simulation was carried out for $Ra = 10^8$, with PCHW boundary conditions, using $A_x = 0.1$ with four Fourier modes in the x direction. Statistics of the flow were recorded and compared with the statistics of the 2-D flow. The most significant difference found was an increase of the heat transfer coefficient in the 3-D flow. For cavities of height aspect ratio 4, the same question was considered in [25]. Experimentally, it was found that in a cavity of $A_x = 1.33$ there is a transition to unsteadiness at $Ra_z \approx 10^8$ (in good agreement with results reported in [14]). Numerical simulations (assuming two-dimensionality) confirmed this result. However, in a 3-D PVBC simulation with a lower Rayleigh number, $Ra_z = 9.6 \times 10^7$, with $A_x = 1$, the flow was found to be 3-D.

These results [24, 25] seem to indicate that for $A_z = 1$ and $A_z = 4$ (and large enough A_x), the flows would never be unsteady and 2-D. But this conclusion is not valid for other aspect ratios: for $A_z = 8$, the critical number for the transition to

unsteadiness is $\mathrm{Ra}_y = 306{,}192 \pm 10$, while the 2-D-to-3-D transition is observed at higher Ra_y numbers, at least $\sim 3.84 \times 10^5$ [26].

Motivation and Summary of the Present Work

The majority of the previous numerical simulations of chaotic and turbulent flows have been carried out assuming 2-D flows. To the knowledge of the authors, there are only two previous 3-D studies: a DHC cavity with AHW and SVW, at $\mathrm{Ra} = 10^{10}$ using a relatively low spatial resolution ($62 \times 122 \times 62$ with QUICK) [23]; and a cavity with $A_x = 0.1$, $A_z = 1$, at $\mathrm{Ra} = 10^8$, assuming PCHW and PVBC, using only four Fourier modes on the x axis [24]. More work seems necessary to evaluate the effect of the fluctuations in the direction orthogonal to the main flow over the averaged 2-D flows.

The main goal of this article is to use direct numerical simulations of DHC to compare the 2-D and 3-D flows in a situation with $A_z = 4$, $A_x = 1$, $\mathrm{Pr} = 0.71$, $\mathrm{Ra}_z = 6.4 \times 10^8$ (i.e., higher than the critical Ra_z number for transition to chaotic regime [14] by a factor of 2.78), using periodic boundary conditions for the 3-D flow (PVBC). The flow configuration chosen, according to the numerical and experimental results of [25] (which are confirmed by our own simulations), is 3-D and time-dependent. It has been selected as an extension to 3-D of one of the 2-D problems studied in [14]. Statistics ($\overline{\mathbf{u}}, \overline{T}, \overline{u_i' u_j'}, \overline{u_i' T'}, \overline{T' T'}$) of the 2-D and 3-D flows are compared. As expected, the 2-D results are in good agreement with the data provided in [14] for $\mathrm{Ra}_z = 6.4 \times 10^8$.

2. GOVERNING EQUATIONS AND NUMERICAL METHOD

Governing Equations

The fluid is considered to be incompressible, Newtonian, and with constant physical properties. To account for the density variations, the Boussinesq approximation is used. Thermal radiation is neglected. Under these assumptions, the governing equations in dimensionless form are

$$\nabla \cdot \mathbf{u} = 0$$

$$\frac{\partial \mathbf{u}}{\partial t} = -\mathbf{u} \cdot \nabla \mathbf{u} + Pr \nabla^2 \mathbf{u} - \nabla p + \mathbf{f} \qquad (1)$$

$$\frac{\partial T}{\partial t} = -\mathbf{u} \cdot \nabla T + \nabla^2 T$$

where the body force vector is $\mathbf{f} = [0, 0, \mathrm{Ra}\, Pr\, T]$. The reference length, time, velocity, temperature, and dynamic pressure used for the dimensionless form are, respectively, L_z, L_z^2/α, α/L_z, ΔT, and $\rho \alpha^2 / L_z^2$. The boundary conditions are isothermal at the vertical walls $\left[T(x, 0, z) = 1, T(x, \frac{1}{4}, z) = 0 \right]$ and adiabatic at the horizontal walls (AHW). Periodic boundary conditions are imposed at the vertical planes $x = 0$ and $x = \frac{1}{4}$ (PVBC). At the four planes $y = 0, y = \frac{1}{4}, z = 0, z = 1$, null velocity is imposed. The initial conditions used are not relevant because the statistics of the flow are

recorded when statistically steady-state behavior is reached. The dimensionless governing numbers are $Pr = 0.71$, $Ra_z = 6.4 \times 10^8$, $A_z = 4$, and $A_x = 1$.* Periodic vertical boundary conditions are used because they allow us to study the 3-D effects due to intrinsic instability of the main flow and not to the boundary conditions. Also, it has to be pointed out that this variant is more convenient from a computational point of view, since the resulting flow has no boundary layers in the x axis and therefore the mesh can be coarser and *uniform* in x. This is an important computational advantage, because Fourier-based methods can be used to solve the Poisson equation.

Numerical Methods

The spatial discretization is carried out using a staggered mesh [27], and a spectro-consistent second-order scheme [28]. In this way the global kinetic energy balance is exactly satisfied even for coarse meshes. For the temporal discretization, a central difference scheme is used for the time-derivative term and a fully explicit second-order Adams-Bashforth scheme for convection, diffusion, and body-force terms. An implicit first-order Euler scheme is employed for the pressure gradient term and the mass conservation equation. Assuming a constant time step, we obtain

$$\frac{\mathbf{u}^{n+1} - \mathbf{u}^n}{\Delta t} = \frac{3}{2}\mathbf{R}^n - \frac{1}{2}\mathbf{R}^{n-1} - \nabla p^{n+1} \tag{2}$$

$$\nabla \cdot \mathbf{u}^{n+1} = 0 \tag{3}$$

where R are the right-hand-side terms of the momentum equation except the pressure gradient. The unknown velocity $\mathbf{u}^{n+1}$ is isolated from Eq. (2) to obtain

$$\mathbf{u}^{n+1} = \mathbf{u}^p - \nabla \tilde{p} \tag{4}$$

where the predictor velocity $\mathbf{u}^p$ is

$$\mathbf{u}^p = \mathbf{u}^n + \Delta t \left(\frac{3}{2}\mathbf{R}^n - \frac{1}{2}\mathbf{R}^{n-1} \right) \tag{5}$$

and the pseudo-pressure is $\tilde{p} = (\Delta t) p^{n+1}$. To determinate $\tilde{p}$, Eq. (3) is imposed:

$$\nabla \cdot \mathbf{u}^{n+1} = \nabla \cdot \mathbf{u}^p - \nabla \cdot (\nabla \tilde{p}) = 0 \tag{6}$$

Combining gradient and divergence operators, we obtain the well-known Poisson equation:

$$\nabla^2 \tilde{p} = \nabla \cdot \mathbf{u}^p \tag{7}$$

*Except a situation where $A_x = 2$ has been considered.

Therefore, the general algorithm for the integration of each time step is:

1. Evaluate $\mathbf{R}^n = \mathbf{R}(\mathbf{u}^n)$.
2. Evaluate $\mathbf{u}^p$ from Eq. (5).
3. Evaluate $\nabla \cdot \mathbf{u}^p$ and solve the discrete Poisson equation.
4. Obtain the new velocity field with Eq. (4).

According to the current state of computing technology, parallel computers are needed for the direct integration of Navier-Stokes equations in turbulent regimes. All the simulations described in this article have been carried out using a low-cost PC cluster. Based on a domain decomposition strategy, the parallelization of the explicit parts of the code is straightforward. However, the efficient solution of the Poisson equations [Eq. (7)], which must be solved almost to machine accuracy, is a critical aspect. This issue is specially relevant if a low-cost PC cluster, with a high latency and low-bandwidth network, is used. Here, a direct Schur Fourier decomposition (DSFD) method is used [29, 30]. The DSFD allows us to solve each Poisson equation [Eq. (7)] almost to machine accuracy (mass residual is reduced by a factor of $\sim 10^{-12}$) using a single all-to-all communication episode. With 36 computing nodes and for a mesh of $N = 64 \times 154 \times 310$ control volumes, the integration of each time step takes roughly 5 s. This is ~ 30 times less than the time needed by a single node (using Fourier decomposition combined with additive correction multigrid [31] to solve the Poisson equations).

Averaging Operator

The main interest of the direct simulation is not the instantaneous fields, but their statistics. In our configuration, after a long enough time from the initial conditions, the flow has the following properties: (1) it is statistically stationary, i.e., all the statistics are invariant under a shift in time; (2) it is statistically 2-D, i.e., its statistics are identical in each yz plane; and (3) it is statistically skew-symmetric, i.e., $\overline{\chi(y,z)} = -\overline{\chi\left(\frac{1}{4} - y, 1 - z\right)}$ for $\chi = \{u_2, u_3, T - \frac{1}{2}\}$

Averages on the three statistically invariant transformations are carried out. For the case of vertical velocity, the averaging operator is

$$\overline{u_3(y,z)} = \frac{1}{2L_x \, \Delta t_a} \int_o^{L_x} \int_{t_o}^{t_o + \Delta t_a} u_3(x,y,z,t) \left(1 + \frac{|u_3(x, L_y - y, L_z - z, t)|}{|u_3(x,y,z,t)|} \right) dtdx \quad (8)$$

The statistic properties of the flow could be estimated only with time (or even space) averaging. However, the triple averaging indicated in Eq. (8) is used in this article with the aim of reducing the averaging period Δt_a needed, and therefore the computational cost. In [24], time and depth averaging but not symmetry averaging are performed. In practice, the evaluation of the averaging operator presents several difficulties. The data to be averaged have to be defined before the simulation, since storage of all the instantaneous fields (about 100 Tbytes) is not possible. The initial instant for the evaluation of the averaging t_0 is not known a priori. The averaging of products of fluctuations such as $\overline{a'b'}$ cannot be evaluated directly and must be postprocessed as $\overline{ab} - \overline{a}\overline{b}$. Since the computing time is long, the computation is

usually interrupted (e.g., by hardware failures in one of the computing nodes), so partial averages of all the products of interest should be saved and then assembled. Symmetry and space averaging cannot be evaluated during the parallel simulation, since this would require massive data exchange between the processors.

3. CODE AND SIMULATION VERIFICATIONS

Code Verification

Before using the code developed for direct numerical simulations, it is necessary to verify its correctness (i.e., that it solves Eq. (1) with the prescribed boundary conditions and the expected order of accuracy). To do so, the method of manufactured solutions (MMS) [32] was used. In the MMS, an arbitrary analytic function $\mathbf{u}_a$ (which will be the solution of the PDE system) is chosen. Then, the source term $\mathbf{f}_a$ that matches with the arbitrary solution is calculated analytically from the PDE to be solved. The initial and boundary conditions are obtained evaluating $\mathbf{u}_a$. This procedure ensures that an analytical solution is obtained even for complex equations such as Navier-Stokes equations. This analytic source term $\mathbf{f}_a$ is evaluated at the discretization nodes and then used as input data for the numerical code. The time-dependent numerical solution $\mathbf{u}_n$ is compared against $\mathbf{u}_a$. The norm of the error is evaluated as

$$\|\mathbf{e}\|_\infty = \|\mathbf{u}_a - \mathbf{u}_n\|_\infty = \mathrm{Max}|\mathbf{u}_a(x_i, y_j, z_k, t_n) - \mathbf{u}_n(x_i, y_j, z_k, t_n)| \qquad (9)$$

where the indices x_i, y_j, z_k, t_n sweep all the spatial and temporal domain. If this measure is repeated for systematically refined grids, $\|\mathbf{e}\|_\infty$ must tend to zero with the expected order of accuracy. In general, it can be expressed as

$$\|\mathbf{e}\|_\infty = C_t \Delta t^{p_t} + C_h \Delta h^{p_h} + \text{higher-order terms} \qquad (10)$$

where C_t and C_h are constants, Δt is the time step, Δh is a measure of the spatial discretization, and p_t and p_h are the orders of accuracy of the temporal and spatial discretizations. The values of p_t and p_h obtained with the code are evaluated separately and compared with the theoretical results. With the discretization schemes implemented in our case, $p_t = p_h = 2$ should be obtained for uniform temporal and spatial discretizations.

For too coarse meshes or too dense meshes, the higher-order terms and round-off errors are respectively dominant in Eq. (10) and second-order behavior is not observed. However, within a wide range of Δh and Δt values, the expected orders of accuracy should be obtained. The results are represented in Figure 2, together with the p_h and p_t that fit best with the numerical values. They are in good agreement with the theoretical orders of accuracy (which, using a spectro-consistent scheme, should be below 2 for nonuniform meshes [28]). To look for all possible errors, this procedure has been repeated for different numbers of discretization nodes, domain sizes in the three axes, and mesh concentration parameters, obtaining analogous results. For an explicit parallel algorithm based on spatial decomposition, it is also important to ensure that the results are strictly independent of the number of processors, since bugs in the halo-update routines may be otherwise undetected.
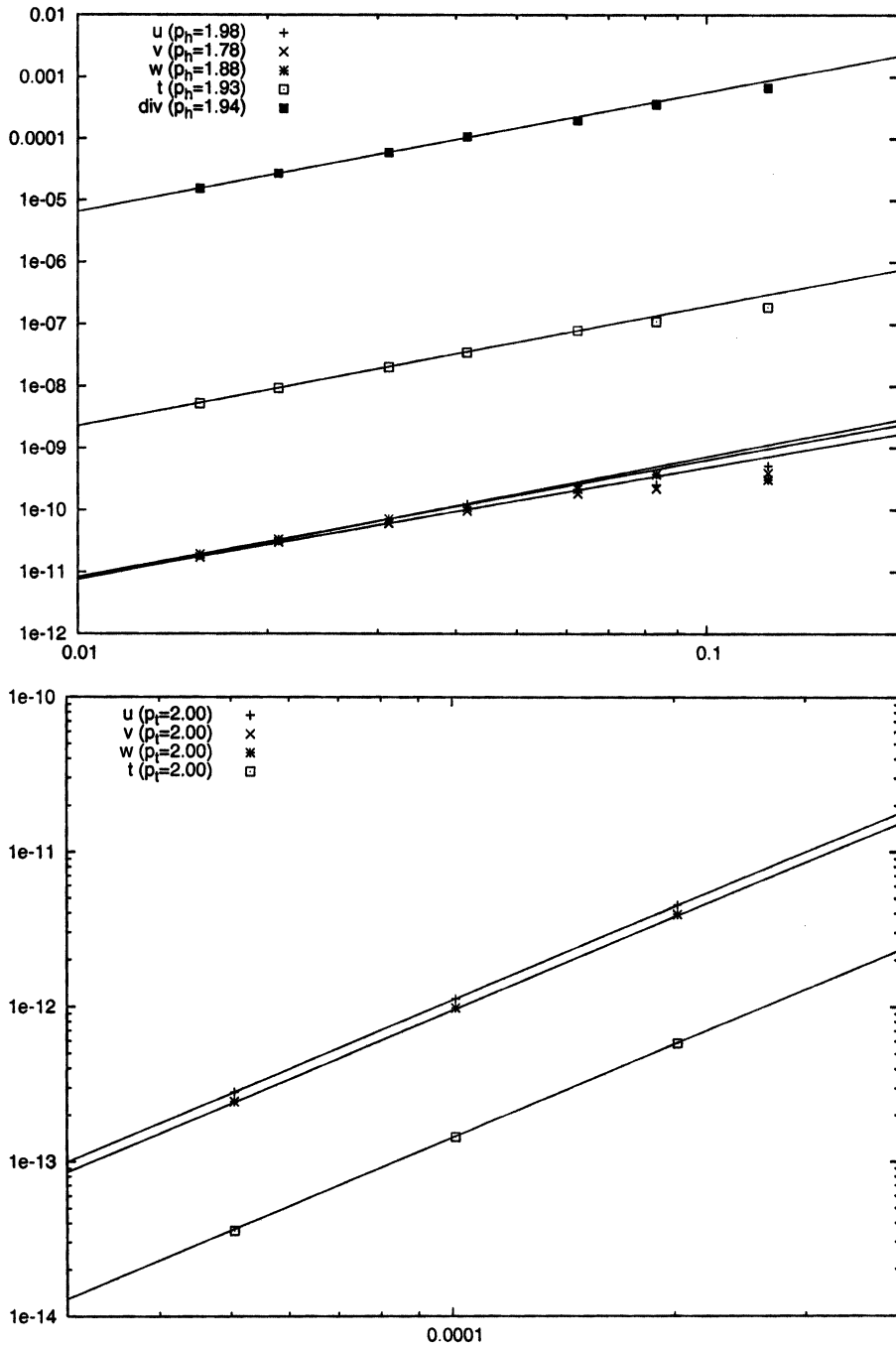
Figure 2. Maximum differences between the analytical and numerical solutions (in the three components of momentum equation, the energy equation, and the divergence operator). Top: errors versus mesh size $\Delta h = L_x/N_x$ for meshes concentrated in axis y and z (with $\gamma = 1.5$), with $N_x = N_y = N_z$. Bottom: errors versus time step. In parentheses (see boxes), the spatial and temporal orders of accuracy (p_h, p_t).

The maximum number of processors used has to be large enough so that all their possible relative positions are exercised. That is, for a 2-D domain decomposition, at least nine processors (3×3) must be used to ensure that one of them has no external boundary conditions. For implicit parallel algorithms (even using direct linear solvers as in our case), slight variations in the results are possible.

Simulation Verification

After the absence of errors in the code has been ensured, it is necessary to determine if the simulation parameters used allow numerical results to be obtained that are reasonably close to the asymptotic solution of the problem. The parameters are mesh size, mesh concentration, time step, domain length in the direction orthogonal to the main flow (L_x), beginning of averaging period t_0, and integration time to evaluate the flow statistics Δt_a. For all of them, a compromise between accuracy and computing time must be accepted.

As the flow under consideration is chaotic, even very small changes in the parameters produce totally different instantaneous fields after a certain integration time. However, the statistical properties of the flow are independent of them. A total of eleven 2-D and 3-D simulations have been carried out and compared in order to estimate the accuracy of the results.

Mesh size and concentration. The selection of an appropriated spatial resolution (number of nodes and concentration) is a critical aspect of direct numerical simulations. In [17] and [15], the spatial resolution was selected using as a guideline the Kolmogorov length scales and the size of the conductive sublayer. In [14], no a priori spatial resolution analysis was needed because, as explained by the authors, the spectral method is unstable if the smallest scales of the flow are not resolved. In our work, a strategy based on successive mesh refinements has been used to obtain a qualitative estimation of the accuracy of the time-averaged 2-D and 3-D solutions. A summary of the 11 simulations carried out is presented in Table 1, where $\overline{\Delta t}$ is the averaged time step. The function used to generate the mesh is

$$y_j = \frac{L_y}{2}\left[1 + \frac{\tanh(\gamma_y\{[2(j-1)/N_y]-1\})}{\tanh\gamma_y}\right] \tag{11}$$

where γ is a concentration factor.

Beginning with the coarsest mesh, referred as C, the number of control volumes in each axis has been multiplied by two and four in meshes B and A, respectively. The concentration parameter is the same, $\gamma_y = \gamma_z = 2$, for meshes B and C. However, due to the CFL condition, it was necessary to decrease it to $\gamma_y = \gamma_z = 1.5$ for mesh A. Mesh A is only slightly finer than mesh B near the boundary layers, but its density is more than double in other areas of the domain. The simulation B2X, analogous to B but with $L_x = 2$ and double the number of control volumes on the x axis, has been carried out to investigate the influence of the domain size in the homogeneous direction. The meshes A2D, B2D, and C2D are a 2-D projection of the respective 3-D meshes A, B, and C. It should be noted that these concentration functions and factors are not necessarily optimal for this problem. In particular, the

Table 1. Main parameters of the 3-D and 2-D simulations

	N_x	N_y	N_z	L_z	γ_y	γ_z	$\Delta y_{\min}$	$\Delta y_{\max}$	$\Delta z_{\min}$	$\Delta z_{\max}$	$\overline{\Delta f}$
A	64	156	312	1	1.5	1.5	4.95×10^{-4}	2.70×10^{-3}	9.75×10^{-4}	5.35×10^{-3}	4.73×10^{-8}
B	32	78	156	1	2.0	2.0	5.08×10^{-4}	6.83×10^{-3}	9.75×10^{-4}	1.35×10^{-2}	5.14×10^{-8}
B2X	64	78	156	2	2.0	2.0	5.08×10^{-4}	6.83×10^{-3}	9.75×10^{-4}	1.35×10^{-2}	5.15×10^{-8}
C	16	39	78	1	2.0	2.0	1.10×10^{-3}	1.40×10^{-2}	2.03×10^{-3}	2.73×10^{-2}	6.25×10^{-8}
A2D	—	156	312	—	1.5	1.5	4.95×10^{-4}	2.70×10^{-3}	9.75×10^{-4}	5.35×10^{-3}	4.89×10^{-8}
B2D	—	78	156	—	2.0	2.0	5.08×10^{-4}	6.83×10^{-3}	9.75×10^{-4}	1.35×10^{-2}	3.17×10^{-8}
C2D	—	39	78	—	2.0	2.0	1.10×10^{-3}	1.40×10^{-2}	2.03×10^{-3}	2.73×10^{-2}	6.25×10^{-8}
AB2D	—	156	312	—	2.0	2.0	2.44×10^{-4}	3.38×10^{-3}	4.78×10^{-4}	6.70×10^{-3}	1.19×10^{-8}
AA2D	—	218	438	—	1.5	1.0	3.48×10^{-4}	1.90×10^{-3}	1.26×10^{-3}	3.00×10^{-3}	2.42×10^{-8}

selection of $\gamma_z = \gamma_y$ might not be the best option. Using the results of the present simulations, better meshes may be used for future work.

A summary of the results is presented in Table 2 and Figure 3. In Table 2, by rows, from top to bottom, the magnitudes are: the total averaged kinetic energy generation ratio $\overline{E_g}$, the total averaged turbulent kinetic energy generation ratio $(Ra/V) \int_\Omega \overline{u_3' T'}\, d\Omega$, the total averaged turbulent kinetic energy dissipation ratio $(1/V) \int_\Omega \overline{\phi(\mathbf{u}')}\, d\Omega$, the overall averaged Nusselt number at the hot wall $\overline{\mathrm{Nu}} = -\int_z (\partial \bar{T}/\partial y)|_{y=0}$, the maximum of the averaged Nusselt number at the hot wall $\overline{\mathrm{Nu}}_{\max} = \mathrm{Max}_z\left[-(\partial \bar{T}/\partial y)|_{y=0}\right]$ and its position, the maxima of $\overline{u_3}$ and $\overline{u_3' u_3'}$ at the central z plane and their respective y positions.

As can be seen in Table 2 and in Figure 3, the differences in the first-order statistics in meshes A and B (in both 2-D and 3-D simulations) are relatively small. However, for the second-order statistics, from the comparison of the results from meshes A and B we cannot conclude that the results of mesh A are accurate enough. To clarify this question, two additional 2-D simulations have been carried out: AB2D with a density double that of B2D in all of the domain; and mesh AA2D, designed to be finer in the areas where the previous simulations indicated larger fluctuations. The results of A2D, AA2D, and AB2D are quite similar even for the second-order statistics (despite their differences in the minimum and maximum control-volume sizes). This seems to indicate that the second-order results of mesh A2D are reasonably accurate. As the distribution of the second-order statistics is more complex (as discussed later) for the 2-D simulations than for the 3-D simulations, we can conclude that the second-order statistics of the 3-D simulations are reasonably accurate too. Nevertheless, simulations with more resolution would be convenient in order to confirm the results presented here. In particular, the mesh density in the periodic direction should be checked. Also, a methodology for quantitative estimations of the accuracy of the first- and second-order statistics would be of high interest.

Time step. As the time discretization of the transport equations is explicit, Δt is limited by the CFL condition. The averaged time step used for each mesh can be found in Table 1. To determinate if Δt is small enough as to obtain independent averaged results, the simulations with mesh B2D have been repeated for time steps two and four times smaller. The results (not included for brevity) indicate that the time steps used are correct.

Domain length in the direction orthogonal to the flow. If PVBC are used, the aspect ratio in the periodic direction A_x must be chosen large enough to contain all relevant large-scale vortices. In order to elucidate whether $A_x = 1$ is enough, the case B was repeated with $A_x = 2$ and the same mesh density. The results obtained are very similar for the first-order statistics but somewhat different for the second-order statistics (Figure 3). This indicates that a box larger in x axis may be necessary.

Integration period Δt_a. In order to estimate the averaging time Δt_a needed to obtain asymptotic statistics, the evolution of several first- and second-order statistics was studied as a function of Δt_a. As expected, the convergence of the first-order statistics is faster. A summary of the results is presented in Figure 4. A similar approach was used in [24], which compared the results obtained with three different integration

**Table 2.** Summary of the 3-D and 2-D results

	A	B	B2X	C
$\overline{E_g}$	4.415×10^{10}	4.421×10^{10}	4.432×10^{10}	4.406×10^{10}
$(1/V)\,\text{Ra}\int_\Omega \overline{u'_3 T'}$	1.341×10^8	1.232×10^8	9.995×10^7	1.842×10^8
$(1/V)\int_\Omega \overline{\phi(u')}$	1.542×10^9	1.330×10^9	1.089×10^9	1.338×10^9
$\overline{Nu}$	4.920×10^1	4.915×10^1	4.918×10^1	4.918×10^1
$\overline{Nu}_{max}$	1.721×10^2	1.722×10^2	1.717×10^2	1.815×10^2
z	4.525×10^{-3}	3.647×10^{-3}	3.647×10^{-3}	3.152×10^{-3}
$\overline{u_3}_{max}$	5.599×10^3	5.607×10^3	5.618×10^3	5.579×10^3
y	7.508×10^{-3}	7.508×10^{-3}	7.508×10^{-3}	7.508×10^{-3}
$\overline{u'_3 u'_3}_{max}$	3.004×10^5	2.701×10^5	1.841×10^5	3.555×10^5
y	1.326×10^{-2}	1.351×10^{-2}	1.351×10^{-2}	1.351×10^{-2}
$\overline{u_3}_{max}$	1.075×10^3	1.096×10^3	1.098×10^3	8.420×10^2
z	6.106×10^{-2}	6.406×10^{-2}	7.207×10^{-2}	3.303×10^{-2}
$\overline{u'_3 u'_3}_{max}$	3.541×10^5	3.862×10^5	4.196×10^5	3.632×10^5
z	1.061×10^{-1}	1.161×10^{-1}	1.231×10^{-1}	6.206×10^{-2}

	A2D	AA2D	AB2D	B2D	C2D
$\overline{E_g}$	4.418×10^{10}	4.415×10^{10}	4.410×10^{10}	4.419×10^{10}	4.383×10^{10}
$(1/V)\,\text{Ra}\int_\Omega \overline{u'_3 T'}$	4.124×10^6	1.855×10^7	1.514×10^7	2.925×10^6	2.259×10^7
$(1/V)\int_\Omega \overline{\phi(u')}$	8.861×10^8	9.161×10^8	9.179×10^8	8.652×10^8	8.605×10^8
$\overline{Nu}$	4.923×10^1	4.921×10^1	4.923×10^1	4.920×10^1	4.949×10^1
$\overline{Nu}_{max}$	1.700×10^2	1.695×10^2	1.686×10^2	1.701×10^2	1.769×10^2
z	4.525×10^{-3}	4.462×10^{-3}	4.476×10^{-3}	3.647×10^{-3}	3.152×10^{-3}
$\overline{u_3}_{max}$	5.640×10^3	5.648×10^3	5.643×10^3	5.640×10^3	5.658×10^3
y	7.508×10^{-3}	7.508×10^{-3}	7.758×10^{-3}	7.508×10^{-3}	7.508×10^{-3}
$\overline{u'_3 u'_3}_{max}$	3.838×10^3	3.852×10^3	4.648×10^3	3.417×10^3	4.343×10^4
y	1.351×10^{-2}	1.401×10^{-2}	4.329×10^{-2}	1.351×10^{-2}	1.351×10^{-2}
$\overline{u_3}_{max}$	1.137×10^3	1.179×10^3	1.152×10^3	1.077×10^3	7.784×10^2
z	8.408×10^{-2}	8.709×10^{-2}	8.609×10^{-2}	8.208×10^{-2}	7.407×10^{-2}
$\overline{u'_3 u'_3}_{max}$	5.779×10^5	5.131×10^5	5.432×10^5	5.440×10^5	4.511×10^5
z	1.562×10^{-1}	1.602×10^{-1}	1.572×10^{-1}	1.502×10^{-1}	8.759×10^{-1}

periods. As an additional control parameter, the dimensionless imbalance of kinetic energy generation ratio, $|\overline{E_g} - \overline{E_d}|/\overline{E_g}$, was also analysed. For $\Delta t_a > 4.5 \times 10^{-2}$, this parameter is of the order of 10^{-5}. To select a Δt_a, as for the other numerical parameters, a compromise between accuracy and computing time must be made. In our case, for all the simulations $\Delta t_a > 2 \times 10^{-2}$, which is in good agreement with the integration period used in [14] for the same Ra number, $\Delta t_a \approx 1.56 \times 10^{-2}$ (expressed in our dimensionless scale).

The integration must begin at $t = t_0$, when the effect of the initial conditions is lost and the flow has reached a statistically stationary state. In order to ensure that a correct t_0 has been selected, two verifications are carried out. First, during the simulation, the evolution of the velocity and temperature at different positions and the overall Nusselt number are controlled. Second, the time integral in Eq. (8) is evaluated beginning at the final instant, $t_0 + \Delta t_a$, and going back until a certain initial instant t, when the statistic values obtained are considered stable. If stable statistics are reached, then we can conclude that the integration period used does not overlap
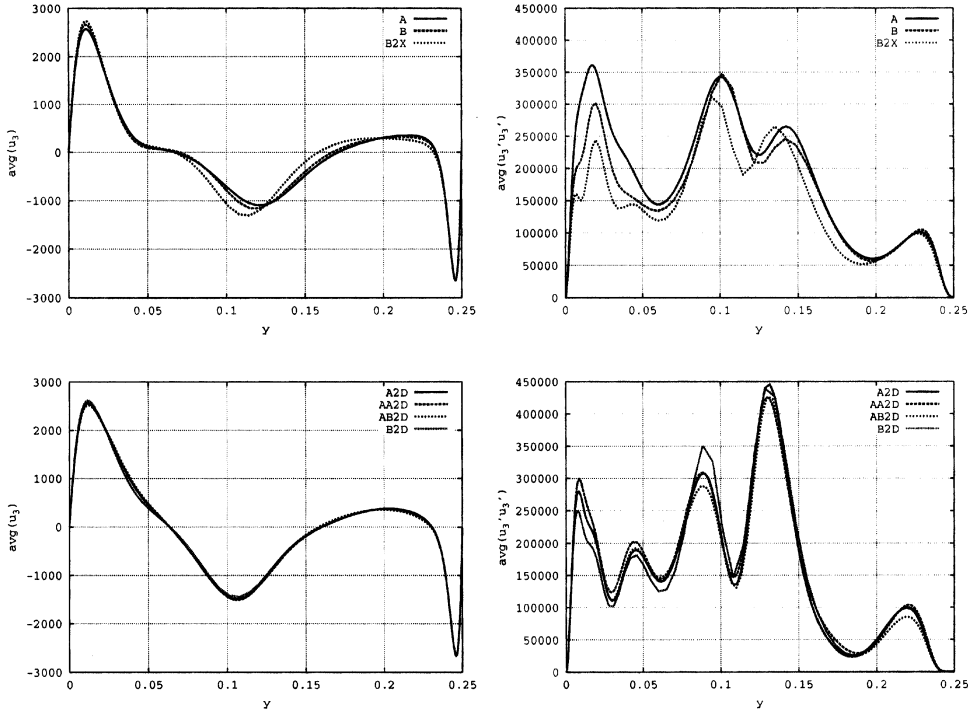
Figure 3. Comparison of the first- and second-order statistics in the section $z = (15/16)L_z$ (where the discrepancies are largest). Top: $\overline{u_3}$ and $\overline{u'_3 u'_3}$ for the 3-D simulations. Bottom: Analogous results for the 2-D simulations.

with the transient period (i.e., $t > t_0$). If stable statistics cannot be obtained, the simulation should proceed, to allow a longer Δt_a.

4.   RESULTS AND DISCUSSION

Instantaneous Fields

The temperature distribution maps of three different instants of the 2-D and 3-D[†] simulations are presented in Figure 5. The main difference is that in the 2-D simulations the chaotic fluctuations are concentrated in the top and bottom areas of the cavity, while the vertical boundary layers are almost totally stable. This can be clearly appreciated in animations of the velocity components and temperature distributions. The second-order statistics confirm this effect, as discussed below. Also, in the 2-D results, the vortices at the end of the vertical boundary layers are more vigorous and stable, as can also be appreciated in the streamline maps of $\overline{\mathbf{u}}$ (Figure 6) Occasionally, in the 3-D simulation, there are large instability episodes, clearly visible in the animations, where the three-dimensional structures generated at the top right and bottom left areas of the cavity propagate across all the boundary layers. A

[†]The results discussed in the next paragraphs correspond to simulations A and A2D.
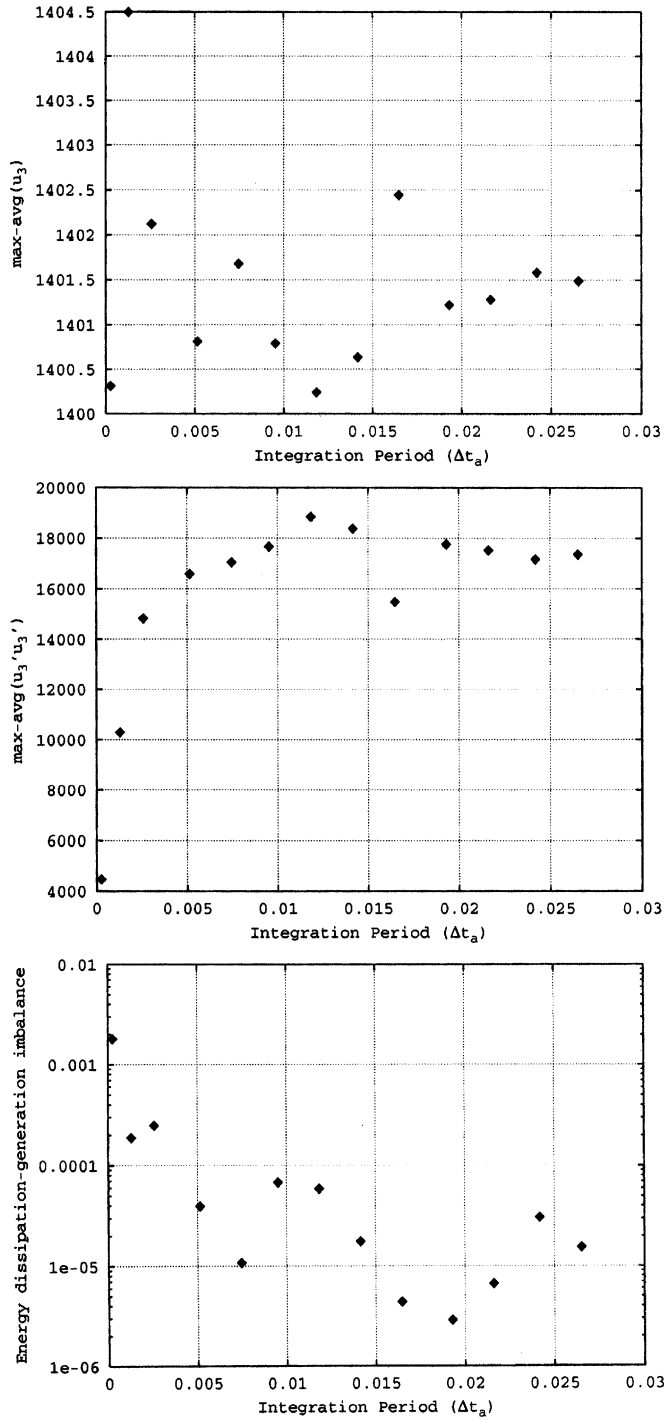
Figure 4. Estimation of the integration period Δt_a needed to evaluate first- and second-order statistics (using simulation parameters B). Top: Maximum $\overline{u_3}$ at the central z plane versus Δt_a. Center: Maximum $\overline{u_3' u_3'}$ at the central z plane Δt_a. Bottom: Accumulation of kinetic energy, $|\overline{E_g} - \overline{E_d}|/\overline{E_g}$ versus Δt_a.
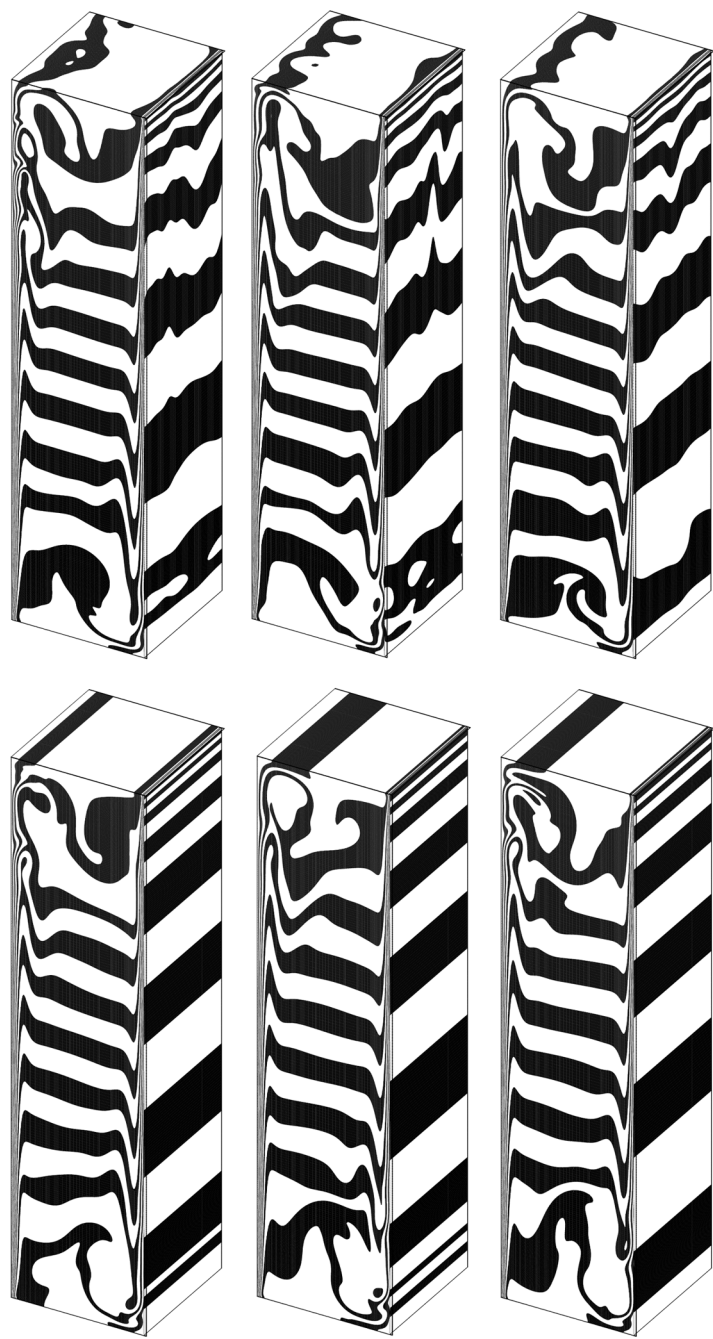
Figure 5. Instantaneous temperature maps corresponding to the statistically steady state, with a vertical section at $y = 0.95 L_y$. Top: Results of the 3-D simulation. Bottom: Analogous results of the 2-D simulation.
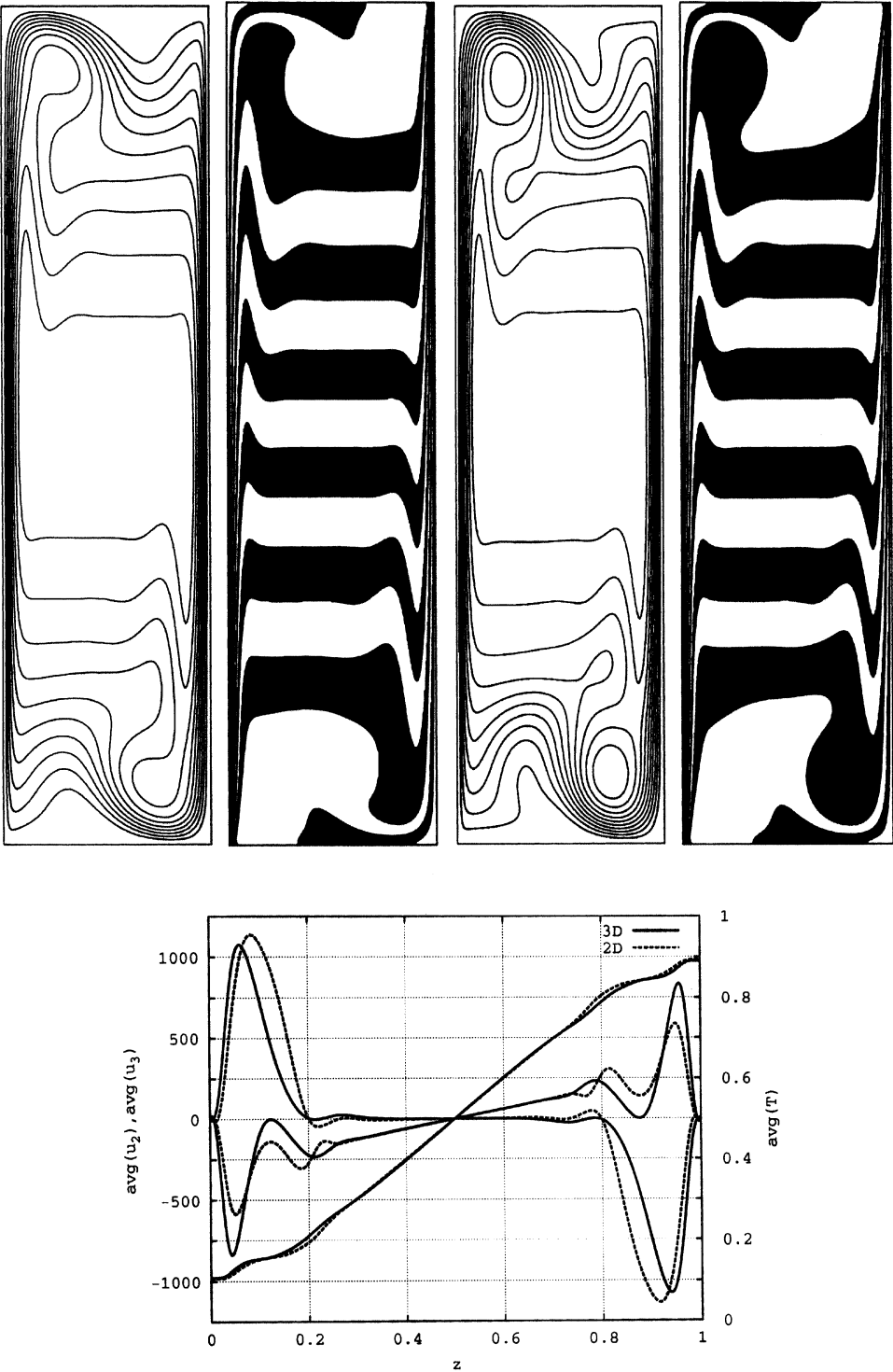
Figure 6. Averaged flow field. Top: From left to right, averaged results of 3-D and 2-D simulation, streamlines and isotherms. Bottom: Vertical profiles at $y = 0.5L_y$ of $\overline{u_2}, \overline{u_3}$, and $\overline{T}$.

physical explanation of this phenomenon, which has not been observed in the 2-D results, is beyond the scope of this article. However, it is too infrequent to generate significant values of $\overline{u_1' u_1'}$ and $\overline{u_2' u_2'}$ at the vertical boundary layers.

Averaged Flow

The averaged flow maps are presented in Figure 6. A quantitative comparison with the results of [14] is difficult, but (as expected) the 2-D results seem to be in good agreement.[‡] Despite the large differences in the instantaneous maps, the 2-D and 3-D averaged flows are similar. In both cases there is a large core area with very low averaged velocity and a stratified temperature distribution. The thermal vertical boundary layers are very similar. However, in the 2-D simulation the recirculation at the corners is clearly stronger.

Heat Transfer

As expected from the similarity between the 2-D and 3-D averaged thermal boundary layers, the overall averaged Nusselt numbers are almost equal, 49.23 for the 2-D case and 49.20 for the 3-D case (see Table 2). The averaged local Nusselt distribution is also very similar, as can be observed in Figure 7. However, there are differences in the instantaneous Nusselt numbers, which are clearly 3-D (Figure 7, bottom left), and the standard deviation of the local Nu number is significantly different in the 2-D and 3-D results (Figure 7, top).

Kinetic Energy Balances

The transport equation for kinetic energy, $e = \frac{1}{2} \mathbf{u} \cdot \mathbf{u}$, is obtained from the scalar product of velocity vector and momentum equation,

$$\frac{\partial e}{\partial t} = -\nabla \cdot (e\mathbf{u}) + \Pr \nabla \cdot [\mathbf{u} \cdot (\nabla \mathbf{u} + \nabla \mathbf{u}^t)] - \Pr \phi - \nabla \cdot (p\mathbf{u}) + \mathbf{u} \cdot \mathbf{f} \qquad (12)$$

where $\phi(\mathbf{u}) = (\nabla \mathbf{u} + \nabla \mathbf{u}^t) : \nabla \mathbf{u}$. The term $-\Pr \phi$ is the kinetic energy dissipation ratio that arises from the viscous forces term $\Pr \nabla^2 \mathbf{u}$. Integration of Eq. (12) in the domain Ω yields

$$\frac{d}{dt} E = \int_{\partial \Omega} [-e\mathbf{u} + \Pr \mathbf{u} \cdot (\nabla \mathbf{u} + \nabla \mathbf{u}^t) + p\mathbf{u}] \cdot d\mathbf{S} + \int_{\Omega} [\mathbf{u} \cdot \mathbf{f} - \Pr \phi] \, d\Omega \qquad (13)$$

where $E = \int_{\Omega} e \, d\Omega$ is the total kinetic energy. The first term, which accounts for the boundary interactions, is null in domains where all the boundaries are either periodic or with null velocity $\mathbf{u}|_{\partial \Omega} = 0$ (or a combination of both as in our case). Considering

---

[‡]In particular, three digits of the overall Nusselt number are equal.
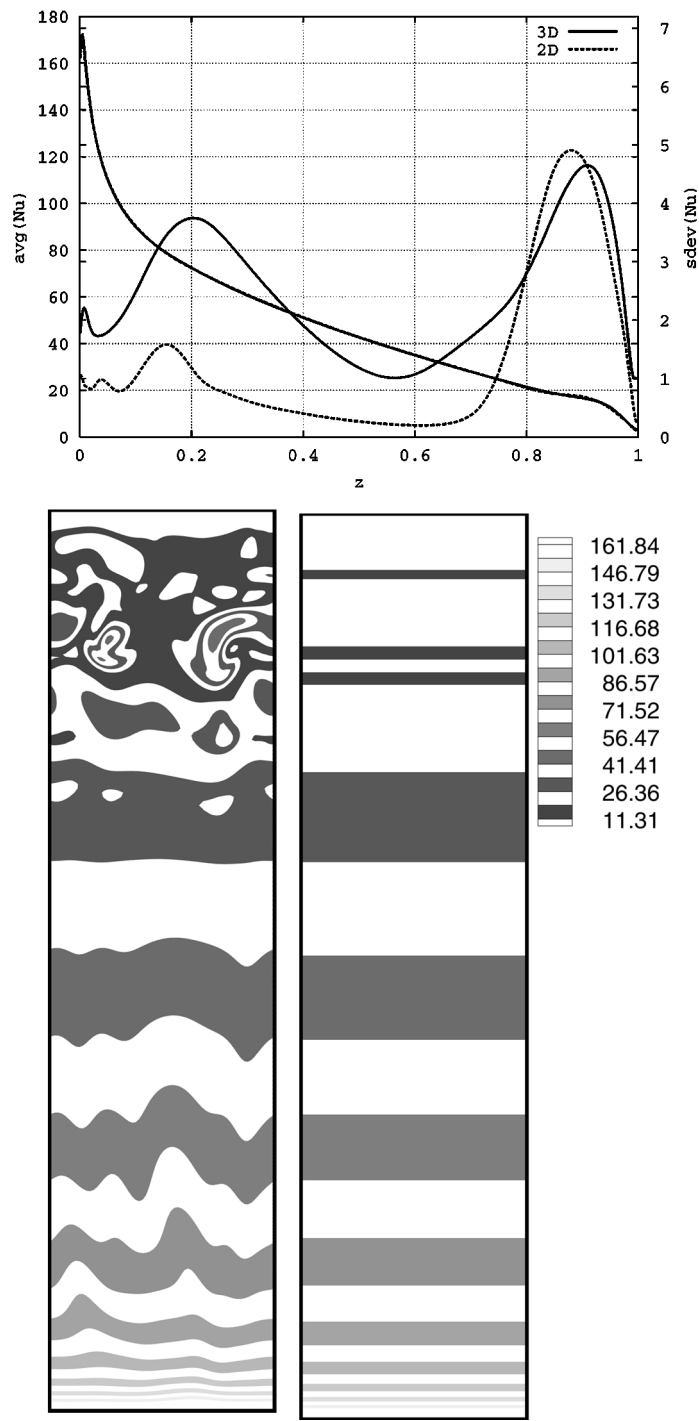
Figure 7. Top: Averaged local Nusselt numbers, $\overline{\mathrm{Nu}}_l = -(\partial \overline{T}/\partial y)_{y=0}$ (at the left), and their standard deviation (at the right) for 2-D and 3-D simulations. Bottom: Instantaneous local Nusselt numbers at the hot wall ($y = 0$) for 3-D (left) and 2-D simulations (right).

these types of boundary conditions, the instantaneous global kinetic energy balance equation can be expressed as

$$\frac{d}{dt}E = \int_{\Omega}(\mathbf{u}\cdot\mathbf{f} - \text{Pr}\,\phi)\,d\Omega = \int_{\Omega}(\text{Ra}\,\text{Pr}\,Tu_3 - \text{Pr}\,\phi)\,d\Omega \qquad (14)$$

It is clear from this expression that the only terms of the momentum equation that contribute to the evolution of the total kinetic energy are -Pr ϕ, which necessarily dissipates kinetic energy to thermal energy (as $\phi \geq 0$), and the body-force term $\mathbf{u}\cdot\mathbf{f}$, which can either generate or dissipate kinetic energy. Pressure gradient and convective terms have a local effect but do not contribute to the global kinetic energy balance. The *spectro-consistent* [28] numerical scheme used for the simulations allows the discrete velocity fields to verify exactly energy balance of the Eq. (14), without introducing any false dissipative effect, even for coarse meshes. This has been tested as an additional verification of the code.

Taking the average [as defined in Eq. (8)] of Eq. (14), for a long enough Δt_a, a global kinetic energy balance is obtained, which, expressed per volume unit, is

$$\underbrace{\frac{\text{Ra}}{V}\int_{\Omega}\left[\overline{u_3}\overline{T} + \overline{u_3'T'}\right]d\Omega}_{\overline{E_g}} = \underbrace{\frac{1}{V}\int_{\Omega}\left[\phi(\overline{\mathbf{u}}) + \overline{\phi(\mathbf{u}')}\right]d\Omega}_{\overline{E_d}} \qquad (15)$$

That is, for a statistically stationary flow, $\overline{E_g}$, the averaged kinetic energy generation rate (due only to the buoyancy forces in our case) must be equal to $\overline{E_d}$, the averaged kinetic energy dissipation rate due to viscous forces. The values of $\overline{E_g}$ obtained in the different simulations can be found in Table 2. Since the instantaneous kinetic energy balances are exactly satisfied, the expression $|\overline{E_g} - \overline{E_d}|/\overline{E_g}$ can be used to control whether t_0 and Δt_a used for the averaging are appropriate. As mentioned before, it has been represented versus Δt_a in Figure 4. The overall kinetic energy generation rate $\overline{E_g}$ is very similar in the 2-D and 3-D simulations, but the turbulent generation term, $(Ra/V)\int_{\Omega}\overline{u_3'T'}\,d\Omega$, and the turbulent dissipation term, $(1/V)\int_{\Omega}\overline{\phi(\mathbf{u}')}\,d\Omega$, differ by factors of 32.6 and 1.73, respectively (see Table 2).

Second-Order Statistics

The distributions of turbulent kinetic energy, its dissipation rate [as defined in Eq. (15)], $\overline{T'T'}$, and $\overline{u_3'T'}$ are presented in Figure 8, while the four non-null components of the Reynolds stress tensors are presented in Figure 9. It should be noted that, as the domain is homogeneous in the periodic direction and the boundary conditions in directions x_2 and x_3 are independent of x_1, all the statistics are independent of x_1, $\overline{u}_1 = 0$, and the fluctuations of u_1 are uncorrelated with the fluctuations of other variables, i.e., $\overline{u_1'u_2'} = \overline{u_1'u_3'} = \overline{u_1'T'} = 0$, except statistical noise that decreases with the integration period. Obviously, the component $\overline{u_1'u_1'}$ is null in the 2-D simulation.

The maxima and spatial distributions of the non-null Reynolds stress sensors are significantly different (i.e., larger than the possible numerical inaccuracies). For the 2-D results, as can be seen in Figures 8 and 9, all the second-order statistics are
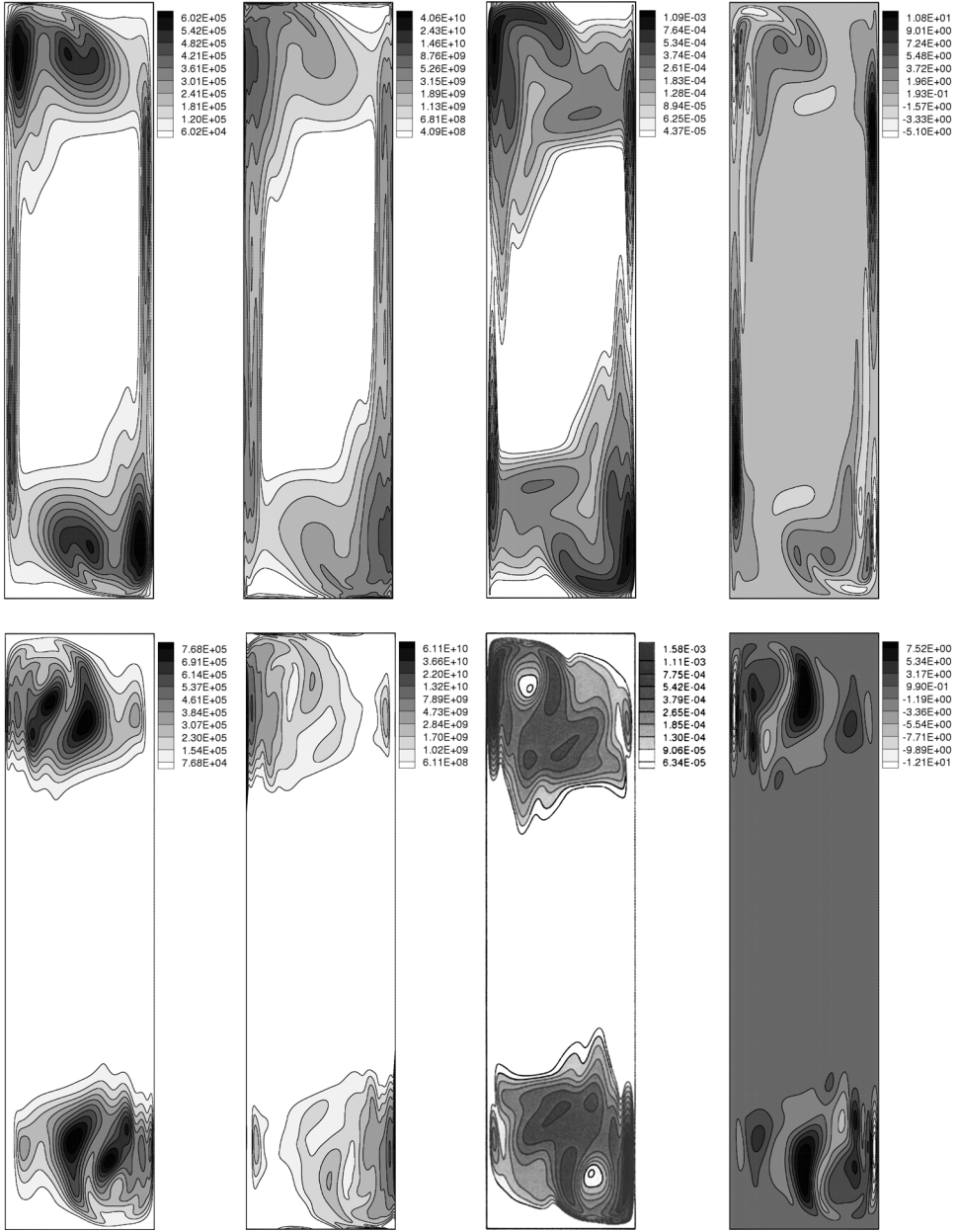
Figure 8. Top: Results of the 3-D simulation, from left to right, $\overline{u_i' u_i'}$, $\overline{\phi(u')T'}$, $\overline{T'T'}$, $\overline{u_3' T'}$. Bottom: Analogous results of the 2-D simulation.

almost null at the vertical boundary layers. This behavior is also observed in the 2-D results presented in [14] for $\mathrm{Ra}_z = 2 \times 10^9$ and $\mathrm{Ra}_z = 10^{10}$. When instantaneous maps are assumed to be 2-D, the vertical boundary layers are almost steady, and the fluctuations are concentrated at the top and bottom regions, where the
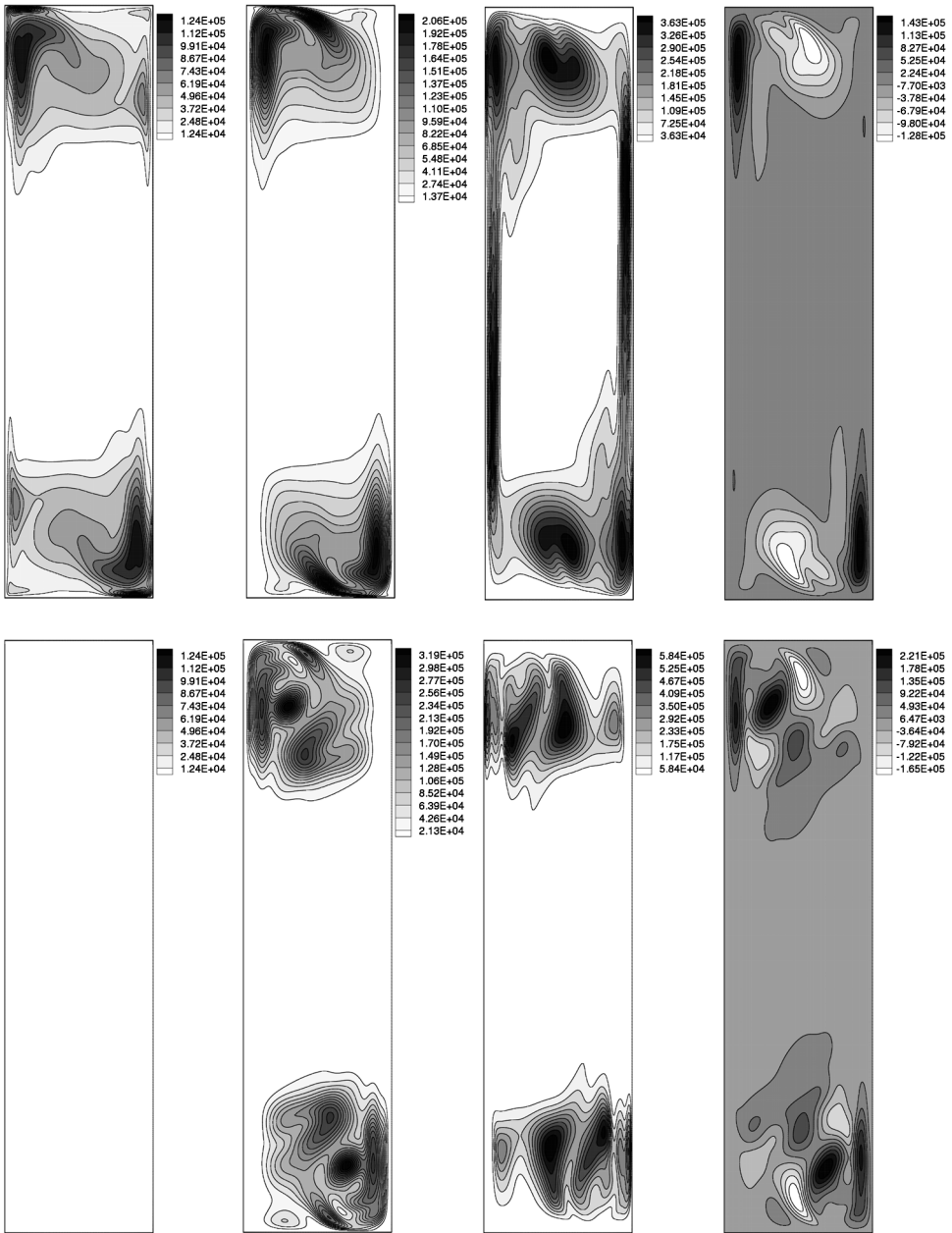
Figure 9. Non-null components of $\overline{u_i' u_j'}$. Top: Results of the 3-D simulation, from left to right, $\overline{u_1' u_1'}$, $\overline{u_2' u_2'}$, $\overline{u_3' u_3'}$, $\overline{u_2' u_3'}$. Bottom: Analogous results of the 2-D simulation.

second-order statistics have more complex distributions than in the 3-D simulations (e.g., the map of $\overline{u_2' u_2'}$ obtained in the 2-D simulation also has a minimum at the corners, not present in the 3-D case). The 2-D and 3-D distributions of $\overline{u_3' T'}$ are totally different.

5. CONCLUSIONS

Results of 3-D and 2-D direct numerical simulations of a buoyancy-driven flow in a differentially heated cavity have been presented. The correctness of the code has been verified using the method of manufactured solutions (MMS), which ensures that the order of accuracy is in good agreement with the theoretical expectation in the whole domain. A low-cost parallel computer (a PC cluster with a conventional 100-Mbits/s network) has been used for the simulations. An explicit scheme has been used for temporal integration and a spectro-consistent second-order scheme for spatial discretization, which preserves the global kinetic energy balances even for coarse meshes. The parallel algorithm is based on spatial domain decomposition. A direct algorithm (DSFD) has been used to solve the Poisson equations with only one communication episode. This method allows high accuracy and efficiency (with speed-ups of about 30), even using a conventional network with high latency and low bandwidth. A detailed description of the flows has been presented, including distributions of the Reynolds stress tensor components, the variance of the temperature, local Nusselt numbers and their standard deviation, and the generation and dissipation of turbulent kinetic energy.

In order to obtain a qualitative estimation of the accuracy of the solutions, a total of 11 direct simulations have been carried out, with different meshes (from 4.8×10^4 to 3.1×10^6 nodes for the 3-D simulations), different integration periods and time steps (up to 2×10^6 time steps), and two lengths in the homogeneous direction of the domain. The accuracy of the first-order statistics seems to be quite good. However, more CPU resources or higher-order numerical schemes would be needed in order to ensure that the second-order statistics obtained for the 3-D flows are accurate enough. With the available data, it seems reasonable to conclude that all the results are at least qualitatively correct. In spite of that, it seems that it would be convenient to use an aspect ratio larger than $A_x = 1$ in the homogeneous direction. The effect of the integration period has been analyzed. The 2-D results are in good agreement with results previously published.

With respect to the comparison of 2-D and 3-D results, their first-order statistics are very similar, in particular, the averaged local and overall Nusselt numbers. This is not the case for the second-order statistics, which are substantially different (by two orders of magnitude in certain cases), far beyond the possible numerical inaccuracies. The assumption of instantaneous 2-D maps influences the distribution of all the second-order statistics. The main differences are at the vertical boundary layers, where the 2-D simulation incorrectly predicts very low values for all the second-order statistics. However, for the Ra number considered, the overall effect of the turbulent fluctuations is relatively small, and this incorrect prediction does not have an important impact on the averaged flow.

If the direct numerical simulations of buoyancy-driven flows are to be used to develop or enhance RANS turbulence models, the assumption of two-dimensionality is not valid, even at the relatively low Rayleigh number considered here. On the other hand, the 2-D simulations may be enough to capture the main features of natural-convection flows, such as the local and overall Nu numbers. However, it is necessary to extend the present results to higher Ra numbers to confirm this conclusion.

REFERENCES

1. G. de Vahl Davis and I. P. Jones, Natural Convection in a Square Cavity: A Comparison Exercise, *Int. J. Numer. Meth. Fluids*, vol. 3, pp. 227–248, 1983.
2. M. Hortmann, M. Peric, and G. Scheuerer, Finite Volume Multigrid Prediction of Laminar Natural Convection: Bench-Mark Solutions, *Int. J. Numer. Meth. Fluids*, vol. 11, pp. 189–207, 1990.
3. P. Le Quéré, Accurate Solutions to the Square Thermally Driven Cavity at High Rayleigh Number, *Comput. Fluids*, vol. 20, pp. 29–41, 1991.
4. M. R. Ravi, R. A. W. M. Henkes, and C. J. Hoogendoorn, On the High-Rayleigh-Number Structure of Steady Laminar Natural-Convection Flow in a Square Enclosure, *J. Fluid Mech.*, vol. 262, pp. 325–351, 1994.
5. D. C. Wan, B. S. V. Patnaik, and G. W. Wei, A New Benchmark Quality Solution for the Buoyancy-Driven Cavity by Discrete Singular Convolution, *Numer. Heat Transfer B*, vol. 40, pp. 199–228, 2001.
6. T. Fusegi, J. M. Hyun, K. Kuwahara, and B. Farouk, A Numerical Study of Three-Dimensional Natural Convection in a Differentially Heated Cubical Enclosure, *Int. J. Heat Mass Transfer*, vol. 34, pp. 1543–1557, 1991.
7. E. Tric, G. Labrosse, and M. Betrouni, A First Incursion into the 3-D Structure of Natural Convection of Air in a Differentially Heated Cubic Cavity, from Accurate Numerical Solutions, *Int. J. Heat Mass Transfer*, vol. 43, pp. 4043–4056, 2000.
8. B. Lartigue, S. Lorente, and B. Bourret, Multicellular Natural Convection in a High Aspect Ratio Cavity: Experimental and Numerical Results, *Int. J. Heat and Mass Transfer*, vol. 43, pp. 3157–3170, 2000.
9. P. Le Quéré, A Note on Multiple and Unsteady Solutions in Two-Dimensional Convection in a Tall Cavity, *J. Heat Transfer*, vol. 112, pp. 965–974, 1990.
10. H.Schweiger, A. Oliva, M. Costa, and C. D. Pérez-Segarra, Numerical Experiments on Laminar Natural Convection in Rectangular Cavities with and without Honeycomb Structures, *Int. J. Numer. Meth. Heat Fluid Flow*, vol. 5, pp. 243–443, 1995.
11. K. H. Winters, Hopf Bifurcation in the Double-Glazing Problem with Conducting Boundaries, *J. Heat Transfer*, vol. 109, pp. 894–898, 1897.
12. R. A. W. M. Henkes, Natural Convection Boundary Layers, Ph.D. thesis, University of Technology, Delft, The Netherlands, 1990.
13. P. Le Quéré and M. Behnia, From Onset of Unsteadiness to Chaos in a Differentially Heated Square Cavity, *J. Fluid Mech.*, vol. 359, pp. 81–107, 1998.
14. S. Xin and P. Le Quéré, Direct Numerical Simulations of Two-Dimensional Chaotic Natural Convection in a Differentially Heated Cavity of Aspect Ratio 4, *J. Fluid Mech.*, vol. 304, pp. 87–118, 1995.
15. M. Farhangnia, S. Biringen, and L. J. Peltier, Numerical Simulation of Two-Dimensional Buoyancy-Driven Turbulence in a Tall Rectangular Cavity, *Int. J. Numer. Meth. Fluids*, vol. 23, pp. 1311–1326, 1996.
16. M. A. Christon, P. M. Gresho, and S. B. Sutton, Computational Predictability of Time-Dependent Natural Convection Flows in Enclosures (Including a Benchmark Solution), *Int. J. Numer. Meth. Fluids*, vol. 40, pp. 953–980, 2002.
17. S. Paolucci and D. R. Chenoweth, Transition to Chaos in a Differentially Heated Vertical Cavity, *J. Fluid Mech.*, vol. 201, pp. 379–410, 1989.
18. S. Paolucci, Direct Numerical Simulation of Two-Dimensional Turbulent Natural Convection in an Enclosed Cavity, *J. Fluid Mech.*, vol. 215, pp. 229–262, 1990.
19. R. J. A. Janssen, R. A. W. M. Henkes, and C. J. Hoogendoorn, Transition to Time-Periodicity of a Natural-Convection Flow in a 3-D Differentially Heated Cavity, *Int. J. Heat Mass Transfer*, vol. 36, no. 11, pp. 2927–2940, 1993.

20. T. Fusegi, J. M. Hyun, and K. Kuwahara, Three-Dimensional Numerical Simulation of Periodic Natural Convection in Differentially Heated Cubical Enclosure, *Appl. Sci. Res.*, vol. 49, pp. 271–282, 1992.

21. R. J. A. Janssen and R. A. W. M. Henkes, Instabilities in Three-Dimensional Differentially-Heated Cavities with Adiabatic Horizontal Walls, *Phys. of Fluids*, vol. 8, no.1, pp. 62–74, 1996.

22. G. Labrosse, E. Tric, H. Khallouf, and M. Betrouni, A Direct (Pseudo-Spectral) Solver of the 2-D/3-D Stokes Problem: Transition to Unsteadiness of Natural-Convection Flow in a Differentially Heated Cubical Cavity, *Numer. Heat Transfer B*, vol. 31, pp. 261-276, 1997.

23. T. Fusegi, B. Farouk, J. M. Hyun, K. Kuwahara, A Direct Numerical Simulation of Periodic Natural Convection in Differentially Heated Cubical Enclosure, in *Proc. Int. Symp. on Engineering Turbulence Modelling and Measurements*, Dubrovnik, Yugoslavia, pp. 261–268, 1990.

24. R. A. W. M. Henkes and P. Le Quéré, Three-Dimensional Transition of Natural-Convection Flows, *J. Fluid Mech.*, vol. 319, 281–303, 1996.

25. F. Penot, A. N'Dame, and P. Le Quéré, Investigation of the Route to Turbulence in a Differentially Heated Cavity, in *Proc. 9th Int. Heat Transfer Conf.*, Jerusalem, pp. 417–422, 1990.

26. S. Xin and P. Le Quéré, An Extended Chebyshev Pseudo-Spectral Benchmark for the 8:1 Differentially Heated Cavity, *Int. J. Numer. Meth. Fluids*, vol. 40, pp. 981–998, 2002.

27. F. H. Harlow and J. E. Welch, Numerical Calculation of Time-Dependent Viscous Incompressible Flow of Fluid with Free-Surface, *Phys. of Fluids*, vol. 8, pp. 2182–2189, 1965.

28. R. W. C. P. Verstappen and A. E. P. Veldman, Symmetry-Preserving Discretization of Turbulent Flow, *J. Computational Physics*, Vol. 187, 343–368, 2003.

29. M. Soria, C. D. Pérez-Segarra, and A. Oliva, A Direct Parallel Algorithm for the Efficient Solution of Incompressible Flow Problems Using Loosely-Coupled Computers, *Numer. Heat Transfer B*, vol. 41, pp. 117–138, 2002.

30. M. Soria, C. D. Pérez-Segarra, and A. Oliva, A Direct Schur-Fourier Decomposition for the Solution of the Three-Dimensional Poisson Equation of Incompressible Flow Problems Using Loosely Coupled Parallel Computers, *Numer. Heat Transfer B*, vol. 43, 467–488, 2003.

31. B. R. Hutchinson and G. D. Raithby, A Multigrid Method Based on the Additive Correction Strategy, *Numer. Heat Transfer*, vol. 9, pp. 511–537, 1986.

32. P. J. Roache, Code Verification by the Method of Manufactured Solutions, *J. Fluids Eng.*, vol. 124, pp. 4–10, 2002.